Engine Thrust Effects on Rocket Aerodynamic Characteristics at High Angle of Attack

William V. Logan,* Roger L. Davis,† and Nesrin Sarigul-Klijn‡
University of California at Davis, Davis, California 95616
and
Marti Sarigul-Klijn§
AirLaunch, LLC, Kirkland, Washington 98033

The results of a numerical investigation of an air-launched rocket's aerodynamic characteristics at low Mach number and high angle of attack, typical of flight conditions just before engine ignition, are presented. Forces and moments on a generic rocket that might be used in an air-launch system are predicted using a validated 3-D Navier–Stokes code. Aerodynamic side and yaw forces are observed to occur under certain conditions with zero degrees sideslip, creating conditions of asymmetric side and yaw forces. Forces such as these have been observed experimentally on a variety of aerospace vehicles. The effects of engine thrust on the aerodynamic side and yaw forces are presented. In addition, the sources of the aerodynamic characteristics under engine-off/on conditions are described. Results show that the nozzle flow from the engine reduces side forces and yaw moments by decreasing separated flow and therefore weakening the asymmetric vortical interactions that cause unstable aerodynamic characteristics.

Nomenclature

A	=	cross-sectional area
C_D	=	drag coefficient
C_F	=	force coefficient
C_L	=	lift coefficient
C_l	=	roll moment coefficient about X axis
C_M	=	moment coefficient
C_m	=	pitch moment coefficient about Y axis
C_n	=	yaw moment coefficient about Z axis
C_Y	=	sideslip coefficient
c	=	speed of sound
d	=	diameter
F_x	=	force coefficient in X direction
F_y	=	force coefficient in Y direction
F_z	=	force coefficient in Z direction
L	=	rocket length
l	=	length of nose cone
ψ	=	angle between resultant and normal force

Subscripts

ref	=	reference conditions
∞	=	freestream conditions

*B.S., Graduate Student, Mechanical and Aeronautical Engineering Department. Student Member AIAA.
†Ph.D., Professor, Mechanical and Aeronautical Engineering Department; davisrl@ucdavis.edu. Associate Fellow AIAA.
‡Ph.D., Professor and Leader of Space Engineering Research and Graduate Program (SpaceED), Mechanical and Aeronautical Engineering Department; nsarigulklijn@ucdavis.edu. Associate Fellow AIAA.
§Ph.D., Chief Engineer for Airdrop. Member AIAA.

I. Introduction

ASYMMETRIC aerodynamic side forces and moments often occur on a variety of aerospace vehicles even though flight conditions are such that no side gusts or sideslip angles are present. Asymmetric forces usually occur at low Mach number and high angle of attack (AOA). The sources of asymmetry have often been traced to the forebody region of the vehicle. Experiments on military fighter aircraft [1], including the F-18 [2–5], F-16 [6,7], and generic fighters [8–10] have been performed at low Mach number and high angle of attack conditions to quantify side forces and demonstrate various control devices that may be used to remove/reduce the aerodynamic sources of asymmetry. Similar sources of asymmetric side forces have been observed experimentally on ogive cylindrical bodies such as rocket nose cones [11].

This paper presents the results of a numerical investigation of an air-launched rocket at low Mach number, high angle of attack, and 0 deg sideslip under engine-off/on conditions. These conditions correspond to those that would exist either just before or immediately after engine ignition. At these conditions, aerodynamic instabilities can occur as a result of side forces generated from asymmetry in the flow vortical structure on the downwind side of the rocket. The effect of engine thrust on these side forces is of particular interest and has also been included in this investigation. Validation of the steady-flow, Reynolds-averaged Navier–Stokes code against experimental data for a nose-cone configuration [12] under the same Mach number and various high angle of attack conditions is included as a demonstration of the capability to accurately predict these flows and regions of aerodynamic side forces.

The results in this paper were derived based on the assumption of steady-state or time-independent flow. The current investigation does not consider the aerodynamic effects while accelerating from free-fall or the time dependency of the nozzle flow after engine ignition. Consideration of dynamic effects would entail an unsteady simulation with time-varying flight conditions requiring significant computer resources. Instead, the present study focuses on predicting the forces and flow physics at the instants just before engine ignition and after engine thrust equilibrium to elucidate how the rocket aerodynamic characteristics change.

II. Numerical Approach

The current approach is to use a 3-D Reynolds-averaged Navier–Stokes procedure, OVERFLOW [13], developed at NASA Ames

Research Center, to determine the steady pressure loads on the rocket at various Mach numbers and freestream conditions. During the current investigation, steady-flow simulations of the rocket, with and without the effects of thrust, were performed at low-speed freestream Mach numbers and at a 60 deg angle of attack to the oncoming flow.

Many previous investigations of rocket aerodynamic pressure loads found in the open literature have been performed using Euler [14–16] (inviscid) solution procedures. Because the Reynolds number of the flow is very high (of the order of 5×10^7), the assumption of inviscid flow might be reasonable and justifiable if flow separation is not present or the location of flow separation is known. The main advantage of using an Euler solution procedure is that without viscous effects, the boundary layer and corresponding high gradients in the velocity field near the surfaces are not modeled. Typical vortex-dominated flows caused by geometry features are well predicted in open literature by Euler simulations because the separation point is fixed. As such, the computational grid and time required to obtain a solution are approximately an order of magnitude less than those that include and resolve the viscous flow. However, flow separation does occur off of the aft surfaces of the rocket, especially at moderate to high angles of attack, which significantly alters the pressure loads on the rocket and can introduce asymmetric side and yaw forces. To eliminate any errors due to neglecting the effects of separation and viscous shear (because the separation location is unknown), the Reynolds-averaged Navier–Stokes equations were solved in the current approach and all viscous flow layers and wakes were resolved. By using a Reynolds-averaged Navier–Stokes solution procedure [15–17], the drag due to viscous shear as well as the effects of the separated flow on the pressure drag can be determined.

The OVERFLOW code solves the Reynolds-averaged Navier–Stokes equations using second-order accurate spatial central differencing and the Spalart–Allmaras turbulence model. The Spalart–Allmaras model [18] was chosen to model the turbulence in the current investigation because of its wide use for strongly inviscid/viscous interacting flows [19], ability to accurately predict the effects of separation compared to other turbulence models [20], and computational efficiency. A blended second- and fourth-order difference dissipation scheme is used to achieve monotonically smooth solutions, capture shocks, and eliminate numerical instabilities. A fully implicit lower/upper symmetric Gauss–Seidel (LU-SGS) relaxation procedure is used to integrate the equations in time. Typical solutions of the rocket in the current investigation converged in 20,000–400,000 iterations depending on the freestream conditions (primarily Mach number) and engine conditions. As the Mach number decreased, the region of separated flow on the downstream surfaces of the rocket increased in size. At very low Mach numbers, the region of separated flow became unsteady and flow shedding was encountered. An adiabatic, no-slip boundary condition was held at all solid surfaces. The wall spacing (distance of first grid point away from the wall) was held at approximately 2×10^{-4} mm. The steady loading on the rocket was determined by considering a fixed upstream Mach number, Reynolds number, angle of attack, and sideslip angle.

III.   OVERFLOW Validation

An experimental investigation was previously conducted at NASA Ames Research Center to measure side forces on forebodies at high angles of attack and Mach numbers [12]. The trade study proved that for various nose cones, separation occurs at the nose rather than the afterbody of the rocket. A single nose cone of similar geometry, the NB2 nose cone, was chosen from the NASA investigation and modeled to validate the results produced by OVERFLOW. The NB2 nose cone has a length to diameter ratio l/d of 2.84 with a 20 deg nose-cone angle. The NB2 nose cone used for NASA's wind tunnel investigation is shown in Fig. 1.

The Reynolds number and Mach number in the wind tunnel experiments were 1×10^6 and 0.25, respectively. Under these conditions, the flow over the NB2 nose cone separated before the end of the cone. Each nose cone in the wind tunnel investigation

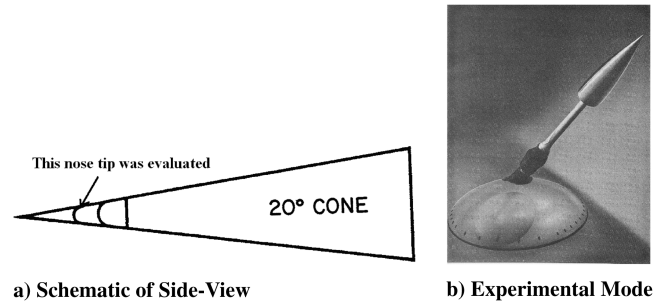a) Schematic of Side-View   b) Experimental Mode

Fig. 1   NB2 nose cone: experimental setup [12].

produced similar results. NASA engineers concluded from these experiments that separation off the rocket at high angles of attack occurs off of the nose rather than off the body. As will be shown later, this conclusion is consistent with the findings from the current investigation.

A computational model of the NB2 nose cone was generated in Chimera Grid Tools, a sister grid-generating program used with OVERFLOW, to validate the results produced in the wind tunnel using the test setup shown in Fig. 1b. The surface grid resolution of 181×92 (circumferential × axial) points was generated by equidistributing points in the circumferential direction and concatenating points in the axial direction to a length of 53.3 cm and diameter of 18.82 cm. The NB2 nose-cone volume computational resolution, which includes the sting, consisted of 70 radial points extending into the far field approximately 160 cm (three nose cone or body lengths) in each direction. The flow boundary conditions (Reynolds number, angle of attack, sideslip angle) were kept consistent with the experimental conditions. The experimental results [12] were analyzed under the assumption of steady flow because no unsteady forces or flow quantities were measured or reported. Typical solutions converged to a fifth-order residual prior 20,000 iterations.

The OVERFLOW predictions are shown vs NASA's experimental wind tunnel data for the nondimensional forces in the Y direction for varying angles of attack (see Fig. 2). The overall trends and absolute levels of side forces are predicted well by OVERFLOW with a region of aerodynamic instability (defined in this investigation as a Mach number region in which side forces occur under flight conditions at zero sideslip) existing at angles of attack between 40 and 80 deg, with the largest asymmetry at 75 deg angle of attack. For each case, the differences between the predicted and the experimental side force coefficient vary at most by a factor of 0.2.

Streamlines off the NB2 nose cone were visualized in FIELDVIEW [21], a data visualization package (see Sec. IV.D), to determine separation and flow symmetry at 75 deg angle of attack. The streamlines separate off the off the NB2 nose cone asymmetrically (see Fig. 4). The interactions of the vortical structures on the aft side of the body at 75 deg angle of attack cause
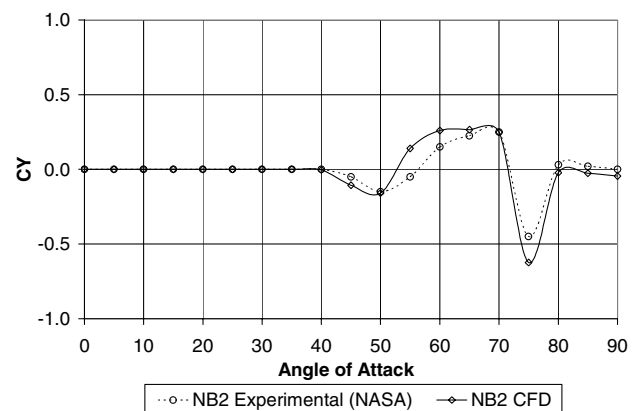

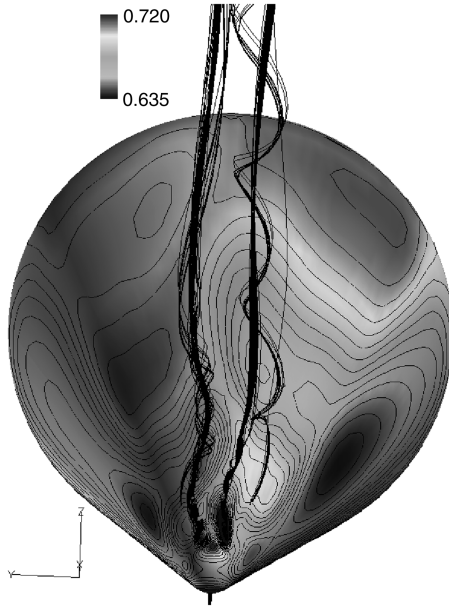Fig. 2   NB2: force in Y vs angle of attack.

Fig. 3   NB2 angle of attack 75 deg: streamlines in X direction and surface pressure contours.
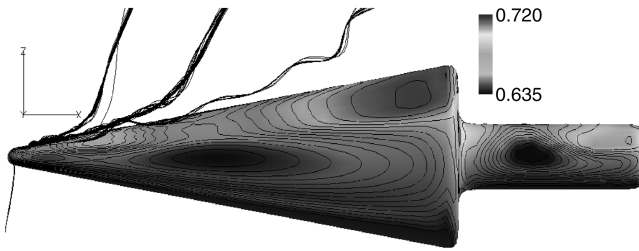

Fig. 4   NB2 angle of attack 75 deg: streamlines in $-Y$ direction and surface pressure contours.

instability in the form of a large force in the Y direction (see Fig. 2). The contours in Figs. 3 and 4 illustrate the fluid pressure on the surface of the rocket. Separation occurs at regions where large adverse pressure gradients exist. Asymmetries in the flow are a result of the strong interaction between the pressure and vorticity fields at and downstream of flow separation. This strong interaction can often come to equilibrium asymmetrically resulting in side forces and yaw moments. The good comparison between predicted side forces and identification of the origin of the side forces with the NB2 nose cone configuration give credence to the use of OVERFLOW for rocket predictions of the same phenomena.

IV.   Configuration

In this section, a description of the grid generation process will illustrate how the 3-D rocket was generated in the Chimera Grid Tools Package. Postprocessing techniques, views, and concepts are also described.

The accuracy of a numerical solution is directly related to the grid density. As the number of grid points increases, the time necessary to compute the solution also increases. Though the most accurate solution is desired, current CPU resources allot for a maximum surface grid size of approximately 1.0×10^6 grid points and a volume grid size not to exceed 8.0×10^6 grid points. In addition to the number of grid points, it is vital to the accuracy of a solution that

Table 1   Zone grid dimensions

Zone name	Circumferential	Axial	Radial
Nose cap	24	24	93
Rocket	121	195	93
Tail cap	22	22	93
Strake 1	36	149	88
Strake 1 top cap	9	57	88
Strake 1 bottom overlap	14	149	75
Strake 1 top overlap	13	129	88
Strake 2	36	149	88
Strake 2 top cap	9	57	88
Strake 2 bottom overlap	14	149	75
Strake 2 top overlap	13	129	88
Rocket nozzle exhaust 1	16	30	16
Rocket nozzle exhaust 2	121	31	67

the grid spacing does not change excessively between adjacent computational grid cells. The surface grid for the rocket was generated by concatenating and equidistributing points, similar to the procedure used for the NB2 nose cone. The grid is uniformly spaced in the circumferential direction, stretched in the axial direction to achieve the curvature of the rocket's geometry, and clustered in the radial direction to capture the viscous flow. The rocket surface grid resolution is 121 circumferential by 195 axial grid points (see Fig. 5 and Table 1).

A.   Rocket Nozzle Exhaust Grid

The exhaust grid (interior to the nozzle for engine-on conditions) was constructed by generating circles at the throat and base of the rocket with points extending in the negative radial direction from the nozzle wall to the X axis. A 3-D grid consisting of $121 \times 31 \times 67$ grid points (see Table 1) was generated by concatenating the two circles in the X direction. This method of grid generation created two points along the X axis with grid singularity, referred to as single axis points. The single axis points were removed and replaced by a second rectangular grid of $16 \times 30 \times 16$ grid points (Table 1). Grid spacing between the two additional rocket nozzle grid blocks and the diverging nozzle was kept consistent.

B.   Rocket Volume Grid

A volume grid for each zone was constructed in Chimera Grid Tools by specifying the boundary conditions, number of points, distance into the far field, initial and end spacing, and smoothing parameters. An average wall spacing of 2×10^{-4} mm was used for each zone of the multigrid rocket, corresponding to an average Reynolds number of approximately 7.93×10^6 (value based on reference diameter). The volume grid was extended into the far field a distance of one rocket length in all directions. Beyond one rocket length, OVERFLOW generated off-body grids [13] extending three rocket lengths into the far field, amounting to a total far-field distance of four rocket lengths. Staying consistent with the surface grid generation, a stretching ratio of 1.2 was used. For each zone, two volume grids were created. The first grid represented the boundary layer extending 10 points with an initial and end spacing of 2×10^{-4} mm. The second grid was stretched (float boundary condition) a distance of one rocket length in the radial direction from an initial spacing of 2×10^{-4} mm to an end spacing of 1.68 m. The rocket grid was periodic in the circumferential direction. The grid spacing of the exhaust grid nozzle was consistent to those of the local rocket grid.

The rocket computational grid size including the far-field grids for engine-off conditions consists of 11 zones amounting to 3,789,030

Fig. 5   Rocket surface computational grid.

grid points. The 13-zone multigrid rocket for engine-on conditions consists of 4,194,316 grid points. The dimensions of the various grid zones that make up the overall computational model are listed in Table 1.

C. Flow Solution and Boundary Conditions

A fixed Courant–Friedrichs–Lewy (CFL) number (nondimensionalized by the length and freestream speed of sound) of 5.0 was used for engine-off conditions. Typical convergence was 20,000–50,000 iterations or 72–120 h using eight CPUs of a Linux cluster. Engine-on conditions called for a fixed CFL number as low as 5×10^{-3} and as high as 0.1. The CFL number was ramped up sequentially as the flow through the nozzle converged, determined by inspecting the residual history. Typical convergence was 200,000–400,000 iterations or 336–672 h using eight CPUs of a Linux cluster. Decreasing the time-step size increased the computational time by increasing the number of iterations to reach convergence. A viscous adiabatic wall was used for all solid surfaces for the engine-off configuration. For the engine-on configuration, the adiabatic wall boundary condition at the base of the rocket was removed. Adiabatic viscous wall boundary conditions were used at the nozzle interior walls representing the exhaust. The rocket and nozzle exhaust grids held circumferential periodic boundary conditions along a single radial plane.

A prescribed temperature, pressure, and Mach number were applied as boundary conditions at the throat of the nozzle to represent 622,751 N of thrust exiting the nozzle. As the geometry of the nozzle diverges after the throat, the flow exiting the throat expands causing an increase in the Mach number and a decrease in pressure and temperature. Shocks and expansion waves can form at the exit of the nozzle due to supersonic exit speeds. By applying the constant throat conditions on the exhaust grid in the nozzle, OVERFLOW calculates the flow through the nozzle and into the far field.

D. Postprocessing

Upon convergence, a subroutine OVERINT of Fomoco Utilities, a postprocessing package included with Chimera Grid Tools, was used to calculate the nondimensional forces and moments about the rocket. OVERPLOT was used to graphically check convergence based on the forces and moments calculated by the OVERINT routine. A utility routine was added to OVERINT to integrate the surface pressure force in all three dimensions to determine the center of pressure over the rocket. The FIELDVIEW [21] scientific visualization package was used to visualize the complex 3-D flow solutions. The surface pressure, vorticity, and velocity contours along with the appropriate streamlines were examined.

V. Results

A series of rocket subsonic flow cases were run in OVERFLOW to analyze the effects that engine-off/on conditions have on the rocket's aerodynamic characteristics at high angles of attack. This was done by predicting the side forces and yaw moments about the rocket at varying Mach numbers at an altitude of 2438.4 m and a 60 deg angle of attack. Mach numbers were varied by 0.05 from 0.05 to 0.60. Side and yaw force instabilities (regions where asymmetric side and yaw forces were predicted under flight conditions at zero sideslip) were determined based on the engine-off results in two Mach number regions: 0.08–0.15 and 0.40–0.50. In these flow regions, figures of the surface pressure, velocity, vorticity, and streamlines were generated in FIELDVIEW [21] to determine what triggers asymmetric side and yaw forces. It was determined that the greatest point of asymmetry within each of the two Mach number regions lie at Mach 0.10 and 0.40. One case at each region of asymmetry was run under engine-on conditions to investigate whether thrust effects can alter the aerodynamic characteristics of the rocket at 0 deg sideslip angle of attack (SSA).
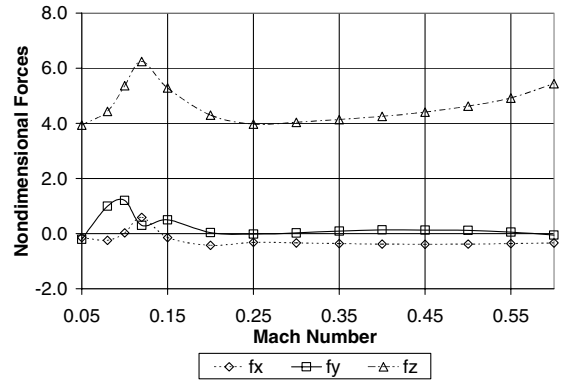

Fig. 6 Nondimensional forces vs Mach number: engine-off conditions.

A. Engine Off

The nondimensional forces in the X, Y, and Z directions are illustrated for 60 deg angle of attack vs the Mach number at engine-off conditions (see Fig. 6). The largest force coefficient in the Y direction in the low Mach number region of instability is 1.207 (2436.1 N) occurring at a Mach number of 0.10. The maximum force coefficient in the Y direction for the smaller high Mach number region of instability equals 0.135 (4353.6 N) occurring at a Mach number of 0.40.

Asymmetric aerodynamic characteristics were determined based on the magnitude of the moments about the leading-edge point of the rocket. The center of gravity of the rocket is located 11.68 m in the axial direction from the nose. The nondimensional moments (roll, pitch, and yaw) are shown for 60 deg angle of attack vs the Mach number for engine-off conditions (see Fig. 7). The yaw moment, acting around the Z axis, was analyzed at both Mach number regions determined from the force coefficient in the Y direction. In the lower Mach number region, a maximum yaw moment coefficient of 0.660 (17, 125.3 N · m) occurs at a Mach number of 0.08. At Mach 0.10 where the largest force in the Y direction occurred, the yaw moment coefficient equals 0.586 (23, 751.0 N · m). One would assume that the largest yaw moment would exist at the same Mach number (0.10) as the largest force coefficient in the Y direction. The streamlines confirmed this hypothesis illustrating more asymmetric and unstable flow at Mach 0.10. At the higher Mach number region of instability, the largest yaw moment coefficient of 0.104 (67, 580.2 N · m) occurs at Mach number 0.40 as suggested by the force coefficient in the Y direction.

In both Mach regions, the rolling moment coefficient, about the X axis, increased to a maximum value of 1.0×10^{-2} (8.53 N · m). The pitch moment coefficient, about the Y axis, increased to a maximum value of -3.334 (-4616.9 N · m) at Mach 0.12, corresponding to the large force in the Z direction. In comparison to the large yaw moment at Mach 0.10, the roll and pitch moments were considered insignificant. These results conclude that the air-launched rocket's asymmetric aerodynamic characteristics are primarily due to the side
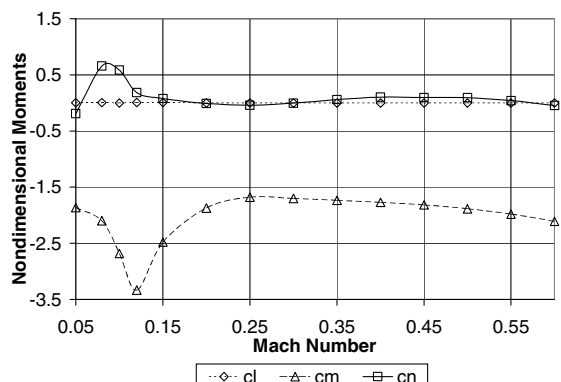

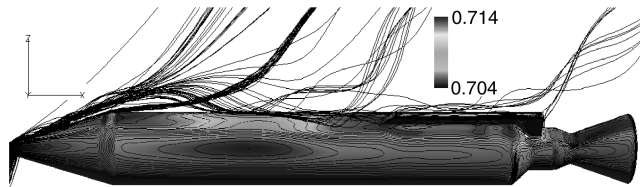Fig. 7 Nondimensional moments vs Mach number: engine-off conditions.

Fig. 8   Mach 0.10 streamlines in $-Y$ direction and surface pressure contours: engine-off conditions.

forces and corresponding yaw moments at 0 deg sideslip angle of attack.

Streamlines were plotted to investigate the unstable vortex structures that cause the asymmetric aerodynamic side and yaw forces on the rocket (see Figs. 6 and 7). At the low Mach number region, a large force coefficient in the Y direction occurred at a Mach number of 0.10, resulting in a large yaw moment. According to the NASA Langley report [12] and the current nose cone study, large forces in the Y direction caused asymmetric separation of the streamlines about the nose and an unsymmetric vortex breakdown to occur. If NASA's conclusion is correct then the streamlines in Figs. 8 and 9 for the air-launched rocket should show the same trends. The streamlines viewed in the negative Y direction separate asymmetrically off the nose and an asymmetric afterbody vortex interaction exists (see Fig. 8). Figure 9 depicts the streamlines viewed in the positive X direction, better illustrating the right-side streamline's different vortical behavior in comparison to the left side.

The current and NASA Langley investigations demonstrate that asymmetric streamlines separate off the nose of the rocket causing side and yaw force asymmetries. The next step was to analyze what causes these asymmetries. The incoming freestream flow expands around the nose of the rocket and the velocity begins to increase to a maximum. The pressure, in contrast to the velocity, decreases to a minimum as seen in the dark regions on the nose of the rocket (see Fig. 9). As the flow expands beyond the nose and the relative minimum pressure point, the pressure begins to increase creating an adverse pressure gradient. The flow due to this pressure gradient initially separates symmetrically off the nose with a core vortex that revolves clockwise on the left side and counterclockwise on the right side (as viewed in the $+X$ direction). This opposite direction rotation leads to an interaction between the left side and right side vortices. A strong vortex interaction resulting from counterrotating vortices causes asymmetric flow on the afterbody of the rocket leading to an asymmetric adverse pressure gradient on the nose. The asymmetric
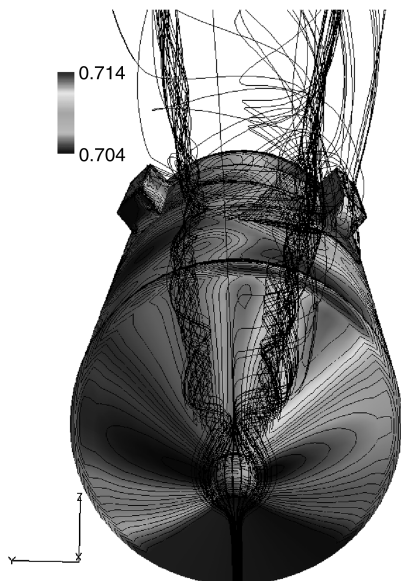

Fig. 9   Mach 0.10 streamlines in X direction and surface pressure contours: engine-off conditions.
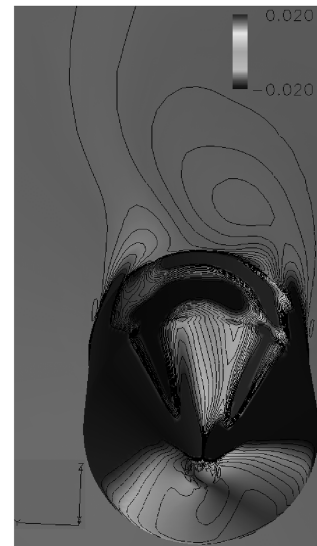

Fig. 10   Mach 0.10 surface axial vorticity contours in X direction: engine-off conditions.

adverse pressure gradient causes the streamlines to separate asymmetrically and an asymmetric vortex interaction. Asymmetric vortex interaction would likely manifest itself as vortex (Strouhal) shedding in an unsteady simulation. However, in the current steady-flow simulations, the asymmetric vortex interaction converges to a fixed, stable state. Aerodynamic side and yaw force instabilities are a result of an asymmetric vortex interaction often referred to as a vortex breakdown.

A vortex breakdown is precisely what occurs at Mach 0.10 under the engine-off condition. As the simulation converges, the streamlines separate asymmetrically. The vorticity at 32% of the rocket's length is illustrated in Fig. 10. At this point along the rocket's body the right-side vortex is larger than the left side. The surface vorticity color contours show alternating patterns on the upper surface of the rocket. The clockwise and counterclockwise axial vorticity originates from the boundary layers underneath and to each side of the rocket. As the flow separates on the aft side of the rocket, the vorticity reaches a critical strength, moves circumferentially in the direction of rotation (i.e., toward the centerline) and then sheds from the surface. The vortices on each side of the rocket alternate with this behavior along the length of the rocket. The streamwise cutting plane streamlines show the vortex streamlines at different points along the length of the rocket (approximately 10, 25, 35, 50, 60, and 70% of the rocket's length) illustrating the alternating left-side and right-side vortical behavior (see Fig. 11).

The asymmetries cause the side forces and yaw moments experienced at Mach 0.10. A force coefficient in the positive Y direction of 1.207 (2436.1 N) acts at the rocket's center of pressure, 10.02 m in the axial direction, relative to the rocket's center of gravity 11.68 m in the axial direction [22]. The rocket experiences a yaw moment in the positive direction of 0.586 (23, 751.0 N · m), which in a transient solution would cause the nose of the rocket from the view in Fig. 10 to rotate to the left about the center of gravity. A time-independent rotation angle ψ (see Nomenclature) was calculated to introduce a measure of sideslip or yaw angle the rocket would experience in a transient solution. The rocket at Mach 0.10 due to the side and yaw asymmetries would encounter a 24.4 deg time-independent rotation angle.

At the high Mach number point of instability (Mach 0.40) the rocket experiences smaller scale asymmetries in comparison to those at Mach 0.10. The flow, similarly, expands around the nose and past a minimum pressure point where the pressure increases. The flow separates symmetrically initially, but a strong vortex interaction between the left-side clockwise rotating and right-side counterclockwise rotating vortices lead to asymmetries in the flow and eventually asymmetric separation off the nose. At steady-state equilibrium, a side force of 0.135 (4353.6 N) acting at the center of
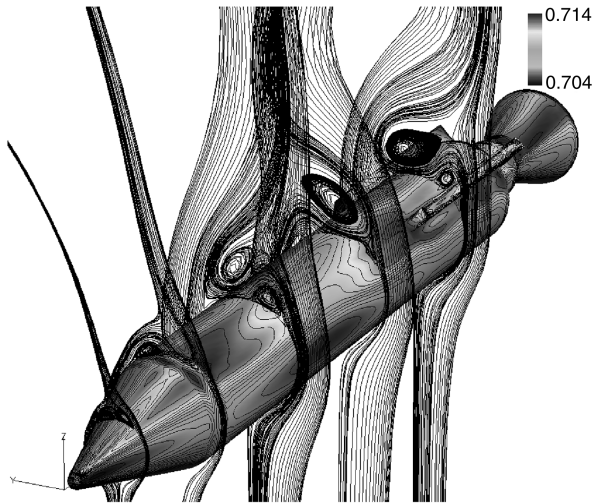
Fig. 11 Mach 0.10 streamlines in isometric direction and surface pressure contours: engine-off conditions.
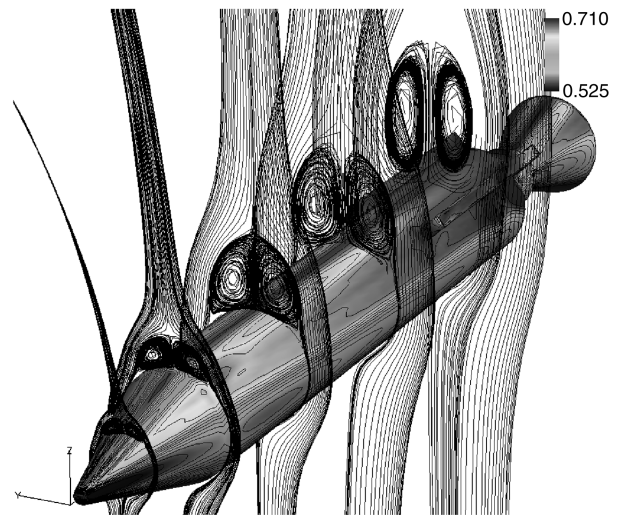

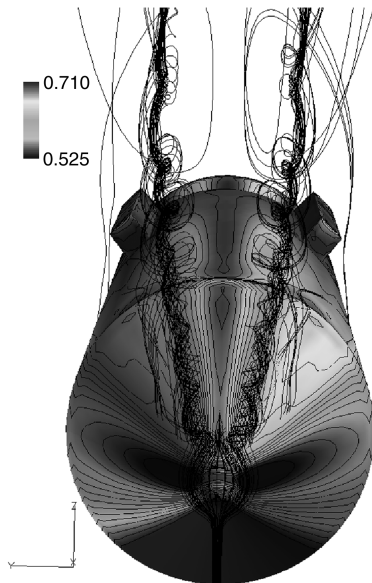**Fig. 13 Mach 0.40 streamlines in isometric direction and surface pressure contours: engine-off conditions.**

Fig. 12 Mach 0.40 streamlines in X direction and surface pressure contours: engine-off conditions.

Fig. 14 Nondimensional forces and moments vs Mach number: engine-on conditions.

pressure 8.33 m from the nose causes a yaw moment of 0.104 (67, 580.2 N · m). The yaw moment leads to a resulting psi rotation angle of 3.14 deg, a more realistic and controllable instability. The vortices (see Fig. 12) illustrate that the right-side vortex is slightly more chaotic in comparison to the left side. The streamwise cutting plane streamlines (see Fig. 13) show a more stable and weaker vortex interaction between the left-side and right-side vortices in comparison to the Mach 0.10 streamlines (see Fig. 11). The weaker vortex interaction explains the smaller side and yaw force asymmetries at Mach 0.40.

B. Engine On

The engine thrust effects on the air-launched rocket are presented in this section. At engine-on conditions (622,751 N of thrust) the rocket was run at both Mach number points of aerodynamic instability to determine if engine thrust would alter the aerodynamic side and yaw force asymmetries. The engine-off/on results are compared for the side force (Y direction) and yaw moment at various flight Mach numbers (see Fig. 14). At Mach 0.10 under engine-on conditions, the rocket experiences a force coefficient in the Y direction of -8.18×10^{-3} (-16.55 N) and a yaw moment coefficient of 4.40×10^{-3} (178.18 N · m), which would lead to a

time-independent rotation angle of -0.002 deg. These engine-on results are reduced in comparison to the rocket under engine-off conditions where a force in the Y direction of 1.207 (2436.1 N) and a yaw moment of 0.586 (23,751.0 N · m) would lead to a time-independent rotation angle of 24.4 deg. At Mach 0.40, engine thrust effects reduced the force in the Y direction from 0.135 (978.73 N) to -4.82×10^{-4} (-15.57 N) and the yaw moment from 0.104
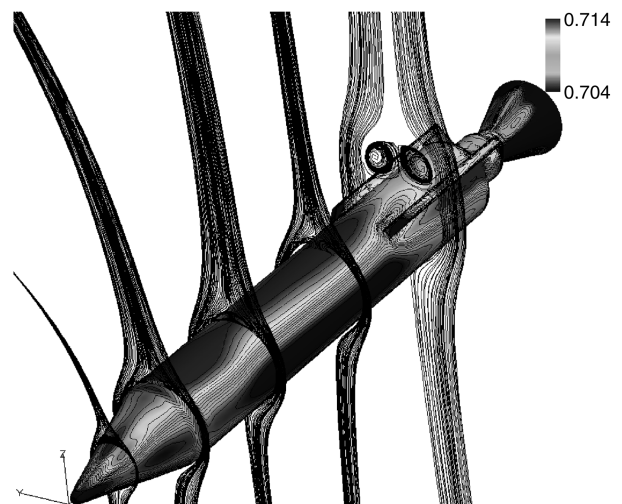

Fig. 15 Mach 0.10 streamlines in isometric direction and surface pressure contours: engine-on conditions.

Fig. 16   Mach 0.10 streamlines in *X* direction and surface pressure contours: engine-on conditions.

Fig. 18   Mach 0.40 streamlines in *X* direction and surface pressure contours: engine-on conditions.

$(67, 580.2 \text{ N} \cdot \text{m})$ to 7.2×10^{-3} $(4675.2 \text{ N} \cdot \text{m})$. The time-independent rotation angle was reduced from 3.14 to -0.001 deg.

The rocket under engine-on conditions experiences relatively zero side and yaw force asymmetries (see Fig. 14). Based on these results and the previous analysis at engine-off conditions, there should be relatively no vortex interaction between the left-side and right-side streamlines. Limited vortex interactions lead to a symmetric adverse pressure gradient and zero side and yaw force asymmetries. The left-side and right-side streamlines at Mach 0.10 in Fig. 15 confirm this conclusion illustrating a symmetric separation and symmetric or stable vortices (see Fig. 15). The streamlines (see Fig. 16) separate off the nose cone of the rocket into two different flow paths. The first path shows stable left-side and right-side streamlines joining and flowing into the far field. A second path of streamlines reattaches to the rocket and interacts with the afterbody strakes, causing the flow to separate symmetrically.

In some flow situations, streamlines can separate asymmetrically on the afterbody of the rocket and cause similar side and yaw force asymmetries as explained under engine-off conditions. One method of combating this occurrence is by introducing afterbody strakes, which can reduce the magnitude of the vortex interaction by changing the position and strength of the vortices. Strakes were
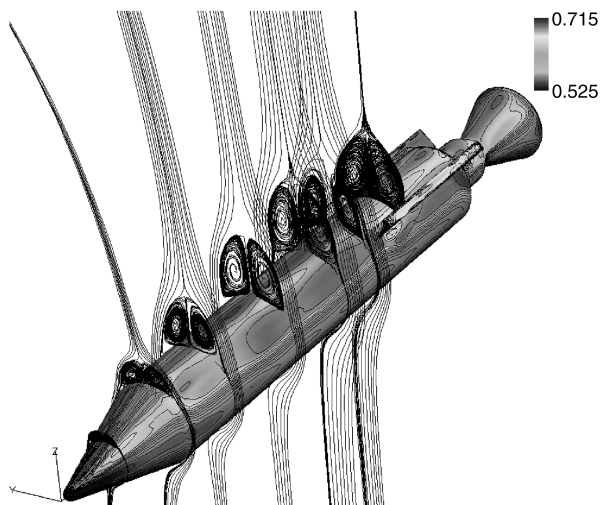

Fig. 19   Mach 0.10 surface pressure contours in *X* direction.

placed on the present rocket in this afterbody position for this purpose.

Symmetric separation and stable vortices are also present with engine-on effects at Mach 0.40. The vortex interaction is weaker than under engine-off conditions retaining symmetric separation and preventing vortex shedding (see Fig. 17). The vortex cores are much tighter with a greater spin, a result of stable noninteracting vortices (see Fig. 18).
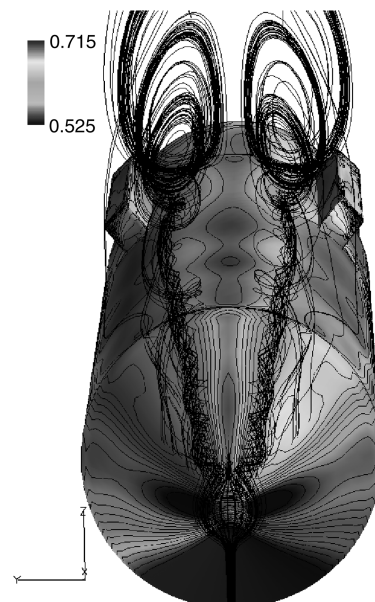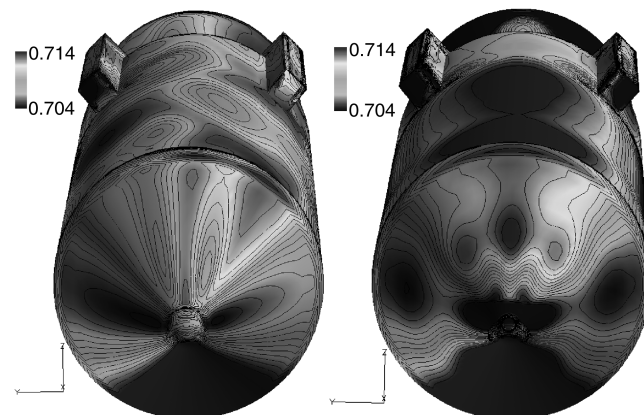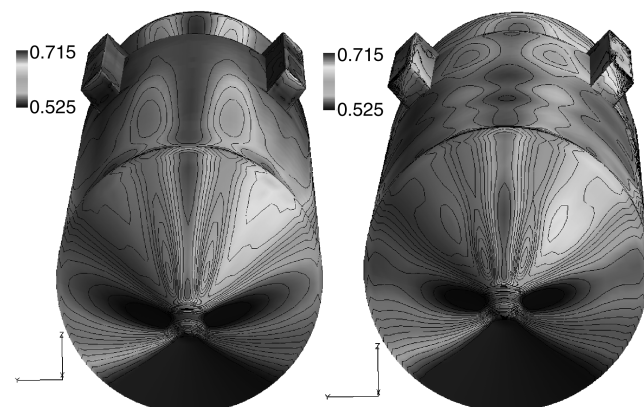

Fig. 17   Mach 0.40 streamlines in isometric direction and surface pressure contours: engine-on conditions.

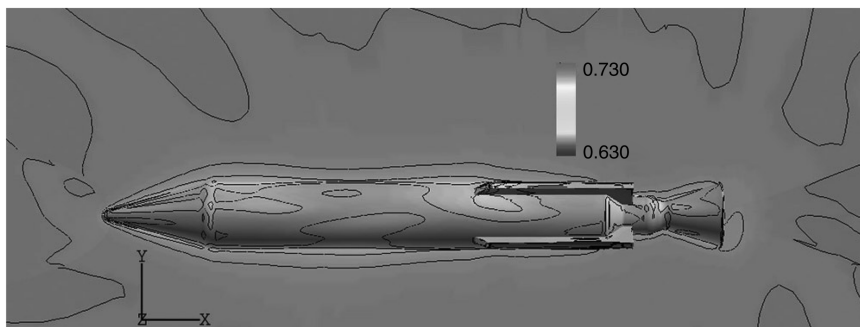**Fig. 20   Mach 0.40 surface pressure contours in *X* direction.**

Fig. 21   Mach 0.10 pressure contours in Z direction: engine-off conditions.
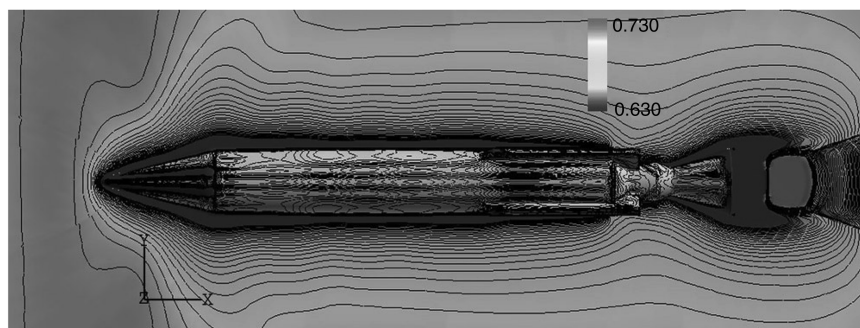

Fig. 22   Mach 0.10 pressure contours in Z direction: engine-on conditions.

Figures 14–18 demonstrate that engine thrust effects more than adequately reduce side and yaw force asymmetries at a 60 deg angle of attack for varying Mach numbers. The explanations as to why thrust effects reduce side and yaw forces have yet to be discussed. The surface pressure plots (see Figs. 19 and 20) for engine-off/on conditions at Mach 0.10 and 0.40 will assist in this discussion. The plume created by the 622,751 N of thrust exiting the nozzle increases the pressure behind the rocket. The high pressure field as a result of engine-plume effects interacts with the incoming freestream pressure field, reducing the surface pressure at the nose and base of the rocket. These effects are shown in the dark regions of the surface pressure plots. The high pressure region on the upper surface of the rocket (see Fig. 19, engine on) is due to the resulting attached flow under engine-on conditions. The pressure field is asymmetric in Figs. 19 and 20 with engine-off conditions and symmetric in Figs. 19 and 20 with engine-on conditions, demonstrating that engine thrust and plume effects greatly reduce the vortex interaction between the left-side and right-side streamlines. The differences in symmetry illustrate the greater aerodynamic side and yaw force asymmetries experienced at Mach 0.10 in comparison to Mach 0.40.

The upper surface and surrounding pressure field plots, viewed in the positive Z direction for Mach 0.10 at engine-off/on conditions (see Figs. 21 and 22), further illustrate that engine-on conditions reduce the side force and yaw moment asymmetries. Side force and yaw moment are directly proportional to the asymmetries in the pressure contours. As seen in Figs. 21 and 22, engine-on conditions reduce the upper surface pressure level of the rocket in comparison to engine-off conditions. A weaker vortex interaction occurs at engine-on conditions leading to symmetric separation off the nose and symmetric upper surface pressure contours. In comparison, the vortex interaction for the engine-off conditions is much stronger, resulting in asymmetric separation off the nose and corresponding asymmetric upper surface pressure contours. The resulting effects from the weaker vortex interaction and symmetric pressure field for the engine-on conditions are reduced side forces and yaw moments.

VI.   Conclusions

Results from a numerical investigation of the aerodynamic characteristics of an air-launched rocket at high angle of attack have

been presented. Validation of the Reynolds-averaged Navier–Stokes code used in this numerical investigation show good comparison with experimental data for a high angle of attack nose-cone configuration with similar vortex phenomena. Regions of asymmetry due to side and yaw forces are predicted to occur on the air-launched rocket in certain Mach number regimes. These asymmetries have been found to result from strong vortical interactions, which cause asymmetries in the flow structure and surface pressure. The engine thrust effects are determined to significantly reduce side and yaw force asymmetries for high angle of attack flow by decreasing the separated flow region on the aft (upper) side of the rocket, therefore weakening the vortical interactions.

References

[1] Malcolm, G. N., "Forebody Vortex Control—A Progress Review," AIAA Paper 93-3540-CP, 1993.

[2] Lanser, W. R., and Murri, D. G., "Wind Tunnel Measurements on a Full-Scale F/A-18 with Forebody Slot Blowing or Forebody Strakes," AIAA Paper 93-1018, 1993.

[3] Ng, T. T., and Malcolm, G. N., "Aerodynamic Control Using Forebody Blowing and Suction," AIAA Paper 91-0619, 1991.

[4] Ng, T. T., Suarez, C. J., and Malcolm, G. N., "Forebody Vortex Control Using Slot Blowing," AIAA Paper 91-3254, 1991.

[5] Ng, T. T., and Malcolm, G. N., "Aerodynamic Control Using Forebody Strakes," AIAA Paper 91-0618, 1991.

[6] LeMay, S. P., Sewall, W. G., and Henderson, J. F., "Forebody Vortex Flow Control on the F-16C Using Tangential Slot and Jet Nozzle Blowing," AIAA Paper 92-0019, 1992.

[7] Suarez, C. J., Malcolm, G. N., and Ng, T. T., "Forebody Vortex Control with Miniature Rotatable Nose-Boom Strakes," AIAA Paper 92-0022, 1992.

[8] Malcolm, G. N., Ng, T. T., Lewis, L. C., and Murri, D. G., "Development of Non-Conventional Control Methods for High Angle of Attack Flight Using Vortex Manipulation," AIAA Paper 89-2192, 1989.

[9] Malcolm, G. N., and Ng, T. T., "Forebody Vortex Manipulation for Aerodynamic Control of Aircraft at High Angles of Attack," SAE Paper 892220, 1989.

[10] Skow, A. M., Moore, W. A., and Lorincz, D. J., "Forebody Vortex Blowing—A Novel Concept to Enhance the Departure/Spin Recovery Characteristics of Fighter Aircraft," AGARD CP-262, May 1979.

[11] Ng, Y. T., Lim, T. T., Luo, S. C., and Lua, K. B., "Effects of Probe

Interference on Side Force of an Inclined Ogive Cylinder," *AIAA Journal*, Vol. 42, No. 2, 2003, pp. 420–423.

[12] Keener, E. R.. Chapmann, G. T., Cohen, L., and Taleghani, J., "Side Forces on Forebodies at High Angles of Attack and Mach Number from 0.1 to 0.7: Two Tangent Ogives, Paraboloid and Cone," NASA TM X-3438, 1977.

[13] Buning, P. G., Chan, W., Renze, K. J., Sondak, D., Chiu, I. T., Slotnick, J. P., Gomez, R., and Jespersen, D., "Overflow User's Manual," NASA Ames Research Center, Moffett Field, CA, 1995.

[14] Priolo, F. J., and Wardlaw, A. B., Jr., "Euler Space-Marching Computations with Crossflow Separation for Missile-Type Bodies," AIAA Paper 1990-616, 1990.

[15] Bulbeck, C. J., Morgan, J., and Fairlie, B. D., "RANS Computations of High-Incidence Missile Flow Using Hybrid Meshes," AIAA Paper 2000-4209, 2000.

[16] Josyula, E., "Computational Study of High-Angle-of-Attack Missile Flows Using Two-Equation Turbulence Models," AIAA Paper 1998-525, 1998.

[17] Birch, T. J., Wrisdale, I. E., and Prince, S. A., "CFD Predictions of Missile Flowfields," AIAA Paper 2000-4211, 2000.

[18] Spalart, P. R., and Allmaras, S. R., "A One-Equation Turbulence Model for Aerodynamic Flows," AIAA Paper 92-0439, Jan. 1992.

[19] Sinha, K., Mahesh, K., and Candler, G., "Modeling the Effect of Shock Unsteadiness in Shock/Turbulent Boundary-Layer Interactions," *AIAA Journal*, Vol. 43, No. 3, March 2005, pp. 586–594.

[20] Godin, P., Zing, D. W., and Nelson, T. E., "High-Lift Aerodynamic Computations with One- and Two-Equation Turbulence Models," *AIAA Journal*, Vol. 35, No. 2, Feb. 1997, pp. 237–243.

[21] "FIELDVIEW User's Manual," Intelligent Light, Rutherford, NJ, 2005.

[22] Dornheim, M. A., "Air Drops Dummy Rocket for DARPA's Falcon," *Aviation Week and Space Technology*, 23 Oct. 2005.

M. Miller
Associate Editor